

PAPER • OPEN ACCESS

Isotope impact on Alfvén eigenmodes and fast ion transport in DIII-D










To cite this article: M.A. Van Zeeland *et al* 2024 *Nucl. Fusion* **64** 056033

View the [article online](#) for updates and enhancements.

You may also like

- [Simulation of the eigenmode spectrum below the Toroidicity-induced Alfvén eigenmode gap generated by the coupling of Alfvén and slow-magnetosonic waves in tokamaks](#)
G J Kramer, C Z Cheng, M Podestà et al.
- [Landau damping of Alfvénic modes in stellarators](#)
Ya I Kolesnichenko and A V Tykhyi
- [Analysis of Alfvén eigenmodes destabilization by energetic particles in TJ-II using a Landau-closure model](#)
J. Varela, D.A. Spong and L. Garcia

Isotope impact on Alfvén eigenmodes and fast ion transport in DIII-D

M.A. Van Zeeland^{1,*} , E. Bass², X.D. Du¹ , W.W. Heidbrink³ , C. Chrystal¹ ,
C. Crocker⁴ , G. DeGrandchamp³ , S. Haskey⁵ , D. Liu¹, J. Gonzalez-Martin³ ,
K.E. Thome¹ , G. Yu⁶  and Y. Zhu⁶

¹ General Atomics, PO Box 85608, San Diego, CA 92186-5608, United States of America

² University of California San Diego, 9500 Gilman Dr, La Jolla, CA 92093-0417, United States of America

³ University of California at Irvine, Irvine, CA 92697, United States of America

⁴ University of California at Los Angeles, Los Angeles, CA 90095, United States of America

⁵ Princeton Plasma Physics Laboratory, PO Box 451, Princeton, NJ 08543-0451, United States of America

⁶ University of California at Davis, Davis, CA 95616, United States of America

E-mail: vanzeeland@fusion.gat.com

Received 8 January 2024, revised 29 February 2024

Accepted for publication 28 March 2024

Published 10 April 2024



Abstract

Measurements of beam driven Alfvén Eigenmode (AE) activity in matched deuterium (D) and hydrogen (H) DIII-D plasmas show a dramatic difference in unstable mode activity and fast ion transport for a given injected beam power. The dependence of the unstable AE spectrum in reversed magnetic shear plasmas on beam and thermal species is investigated in the current ramp by varying beam power in a sequence of discharges for fixed thermal and beam species at fixed density. In general, a spectrum of Reversed Shear Alfvén Eigenmodes (RSAEs) and Toroidal Alfvén Eigenmodes (TAEs) are driven unstable with sub-Alfvénic D beam injection while primarily only RSAEs are driven unstable for the H beam cases investigated. Further, for a given beam power, the driven AE amplitude is always reduced with H beams relative to D and for H thermal plasma relative to pure D or mixed D/H plasmas. Estimates of the fast ion stored energy combined with modeling using the hybrid kinetic-MHD code MEGA indicate that the dominant mechanism contributing to the difference between H and D beam drive is the faster classical slowing down of H beam ions relative to D and the resultant lower beam ion pressure. Calculations of the AE induced stored energy deficits using the reduced critical gradient model TGLFEP show quantitative agreement with the observed dependencies on injected power, isotope and minimum safety factor.

Keywords: fast ions, Alfvén eigenmodes, energetic particles, tokamaks, DIII-D tokamak, isotopes, neutral beam heating

(Some figures may appear in colour only in the online journal)

* Author to whom any correspondence should be addressed.



Original Content from this work may be used under the terms of the [Creative Commons Attribution 4.0 licence](https://creativecommons.org/licenses/by/4.0/). Any further distribution of this work must maintain attribution to the author(s) and the title of the work, journal citation and DOI.

1. Introduction

Fast ion transport by Alfvén Eigenmodes (AEs) is a key limiting factor in high- q_{\min} steady-state discharges [1, 2] and recent predictions raise a similar concern for ITER scenarios [3]. DIII-D experiments investigating these instabilities have formed the basis for several international multi-code EP validation cases [4, 5]; however, the vast majority of these data are for deuterium beams into deuterium background plasmas. In contrast, ITER and all burning plasma experiments will have multiple thermal species (deuterium (D), tritium (T), helium (He)) and at least 1–2 fast ion species such as D beams, 3.5 MeV alphas, hydrogen (H) RF-tails. Indeed, scenario development in future reactors will initially take place during a non-nuclear phase with primarily H and/or He thermal and fast ions, while the eventual thermonuclear plasma will consist of primarily D and T. It is known that both the fast ion and background species can have a dramatic impact on AE stability. In fact, several competing effects that depend on beam ion and thermal species occur simultaneously which can significantly modify AE drive and fast ion transport. Modes are driven by fast ion pressure gradient (∇P_{fast}) [6] and P_{fast} is related to the fast ion slowing down time ($\tau_{\text{se}} \propto M_{\text{fast}}$) [7], where M_{fast} is the fast ion mass. Wave particle resonances depend on Alfvén Mach number ($V_{\text{fast}}/V_A \propto (M_{\text{therm}}/M_{\text{fast}})^{1/2}$), with the strongest interaction occurring for $V_{\text{fast}}/V_A \approx 1$. The most unstable mode ($n_{\text{max}} \propto 1/M_{\text{fast}}^{1/2}$) depends on fast ion ρ^* or banana width which plays a role in stability as well as transport [8, 9, 11]. Multiple EP species, as expected in reactors, further complicate the interaction. An excellent example of this is from TFTR DT experiments, where despite 25+MW of D/T beam power combined with a significant 3.5 MeV alpha population, AEs were stable during the highest power phase and were only unstable after beam ions slowed down [10]. The ≈ 100 kV beam ions stabilized the same modes the alphas were driving, an effect that can be attributed to the beam ion energy gradient ($dF/dE < 0$) damping of the mode overcoming the spatial drive terms from the beam ions and alphas, the competition between which depends on details of the orbit types and modes [11]. Experimentally, large variations in AE amplitude and damping with both plasma and fast ion isotope have been documented [8, 12–16], primarily in plasmas with monotonic magnetic shear. To make accurate and reliable predictions for future devices, it is crucial to expand the range of conditions investigated and validate models for both mode stability as well as fast ion transport that are capable of resolving these complicated sensitivities and interactions.

In this work, beam driven AE activity in matched D and H as well as mixed H/D DIII-D plasmas with varying levels of injected beam power are investigated in reversed magnetic shear plasmas. In support of the experiment, predictions for the impact of Alfvénic activity were made, well before the experiment took place, using the TGLFEP+Alpha model [3, 17] combined with TRANSP/NUBEAM [18, 19]—a so-called ‘predict first’ experiment. TGLFEP+Alpha is a reduced and computationally inexpensive model of EP transport that relies

on the assumption of critical-gradient AE transport with the critical EP density gradient determined by linear AE stability calculations in the TGLF gyro-Landau fluid code [20, 21]. TRANSP/NUBEAM is a Monte Carlo code that computes the time-dependent deposition and slowing down of the fast ions produced by NBI, taking into consideration beam geometry and composition, ion-neutral interactions (atomic physics) and finite Larmor radius effects. TRANSP also includes the ability to accept a radial, pitch and energy dependent anomalous fast ion diffusivity to simulate the effects of MHD and other loss mechanisms. The simulation cycle begins with a ‘classical’ TRANSP run, for a given set of experimental conditions, which forms the inputs for a TGLFEP+Alpha calculation. In this paper, ‘classical’ refers to neoclassical fast ion behavior influenced only by collisional processes and other standard loss mechanisms including charge exchange, i.e. not including wave-induced fast ion transport. TGLFEP+Alpha then yields a radially dependent fast ion diffusivity profile that is used in another TRANSP run to predict the relaxed fast ion profile and impact on other quantities such as DD neutron emission, heating, etc. Predictions for these experiments were made using the same target discharge as the actual experiment—the well documented AE validation case, DIII-D L-mode current ramp discharge 159243 [5, 22]. Discharge conditions will be described in detail in section 2. Predictions focused on the impact of variation of beam power, species, and minimum safety factor (q_{\min}), all of which were varied in the experiment described here. Figure 1 shows the impact of AEs on fast ion pressure (figure 1(a)) and stored energy (figure 1(b)) predicted by TGLFEP+TRANSP. In addition to significant transport (up to 55% deficit in fast ion pressure and 40% in stored energy for the highest D beam injection into D thermal plasma, $D_{\text{NBI}} \rightarrow D$) several predicted trends are apparent in these figures. (i) With respect to isotope, H beam injection has lower expected transport for a given beam power in all cases, (ii) H beam injection into H thermal has the lowest transport of all cases and (iii) the impact of the instabilities is significantly reduced as q_{\min} is varied from 4 to 3. These trends (as well as a quantitative comparison with the mode impact on stored energy as species and power) are compared with experiment in section 5.

Experimentally, as in the predictions, the data show a dramatic difference in unstable mode activity between the various isotope combinations for a given injected beam power, with much weaker mode activity and fast ion transport for all cases with H beams. For the conditions investigated, the data indicate that the dominant mechanism contributing to the difference between H and D beam drive is the faster classical slowing down of H beam ions relative to D and the resultant lower beam ion pressure / AE drive—a result consistent with previous experiments in monotonic shear plasmas showing weaker or no AE activity with H beam injection [8, 13]. This paper is organized as follows. In section 2, the experimental conditions and approach are discussed, then section 3 compares spectra of the unstable mode activity followed by a quantitative analysis of the dependence of mode amplitude on injected power, fast ion beta (β_{fast}), and q_{\min} . Section 4 discusses numerical

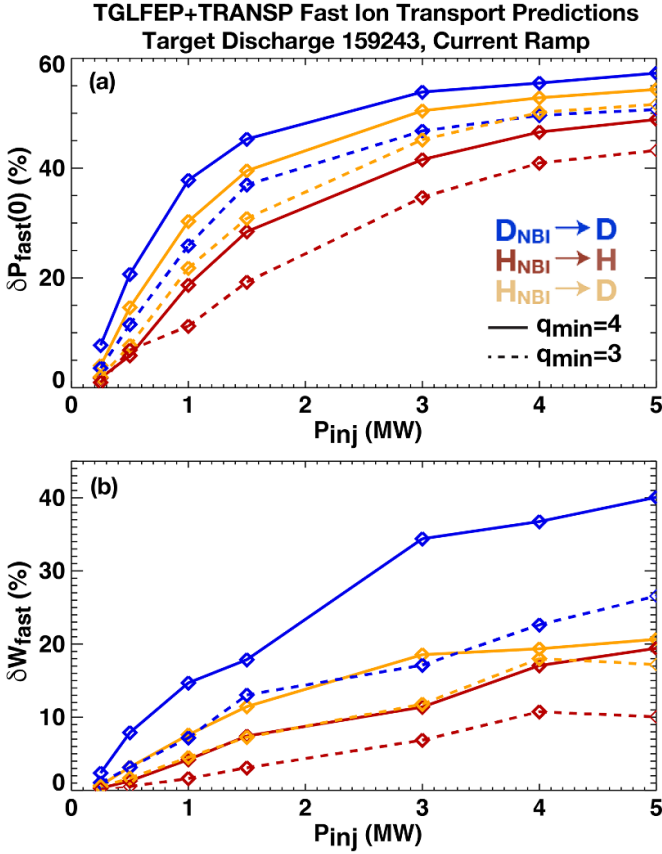


Figure 1. TGLFEP+TRANSP fast ion transport predictions for a beam power scan using DIII-D reversed magnetic shear discharge 159243 during current ramp at $t = 520$ ms ($q_{\text{min}} = 4$) and $t = 800$ ms ($q_{\text{min}} = 3$) as a target. (a) Predicted fast ion pressure and (b) Fast ion stored energy deficit from classical.

simulations of the β_{fast} and q_{min} dependencies using the MEGA code [23]. Section 5 shows the measured impact of the driven EP instabilities on fast ion content, including comparisons with TGLFEP+TRANSP modeling.

2. Discharge background and experimental approach

The dependence of the unstable AE spectrum on beam and thermal species was studied in the plasma current ramp by varying the beam power in a sequence of discharges for fixed thermal and beam species with a nominally fixed density trajectory. The discharges presented utilize an oval (elongation, $\kappa \approx 1.5$) shaped L-mode plasma modeled after two very well documented D discharges used previously for the investigation of beam driven AEs in DIII-D (142111 and 159243) - both have been studied and modeled extensively [4, 5]. In these $B_T = 2.05$ T discharges, 70–80 kV sub-Alfvénic neutral beam injection begins at $t = 300$ ms and continues while the plasma current (I_p) is ramping up at a constant rate of 0.8 MA s^{-1} until reaching approximately 0.8 MA at $t = 600$ ms. The evolution of the various discharge quantities for H injection into a H thermal plasma (red) and D injection into a D thermal plasma (blue)

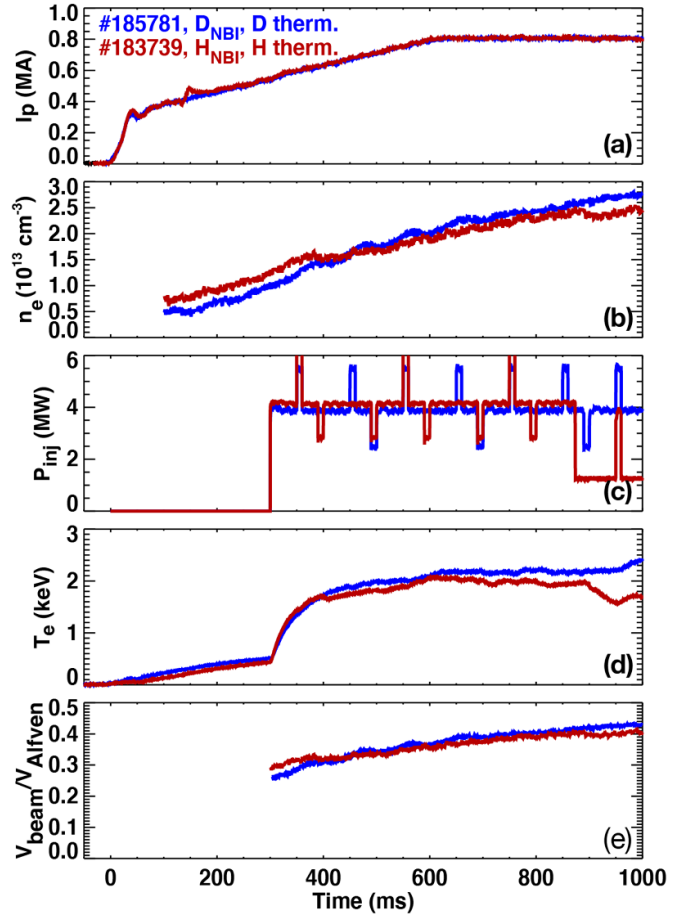


Figure 2. DIII-D discharges 185781 (D_{NBI} , D_{therm}) and 183739 (H_{NBI} , H_{therm}) (a) Plasma current, (b) line-averaged electron density, (c) injected beam power, (d) On-axis electron temperature from ECE and (e) Alfvén Mach number. An example equilibrium is shown in figure 6(a).

(blue) are presented in figure 2. The electron density plays a key role in the presented results (see figure 10) and the pre-programmed trajectory was kept constant for all discharges; one can see the resulting trajectories are matched reasonably well for D/H during the current ramp portion (figure 2(b)). The electron temperature evolution is also close although the actual values depend on the details of both thermal transport (which also has a mass dependence) as well as the fraction of beam power heating the ions vs. electrons which also has a mass dependence. Due to using the same thermal and background mass for the cases shown in figure 2 as well as a reasonably matched density, the resulting ratio of beam to Alfvén speed is also very similar (figure 2(e)) and typically begins $V_{\text{beam}}/V_A \approx 0.3$ and reaches $V_{\text{beam}}/V_A \approx 0.5$ during the period of interest.

3. Impact of isotope on AE activity

Early neutral beam injection during the current ramp phase produces a variety of Alfvénic activity including Toroidicity induced Alfvén Eigenmodes (TAEs) and Reversed Shear

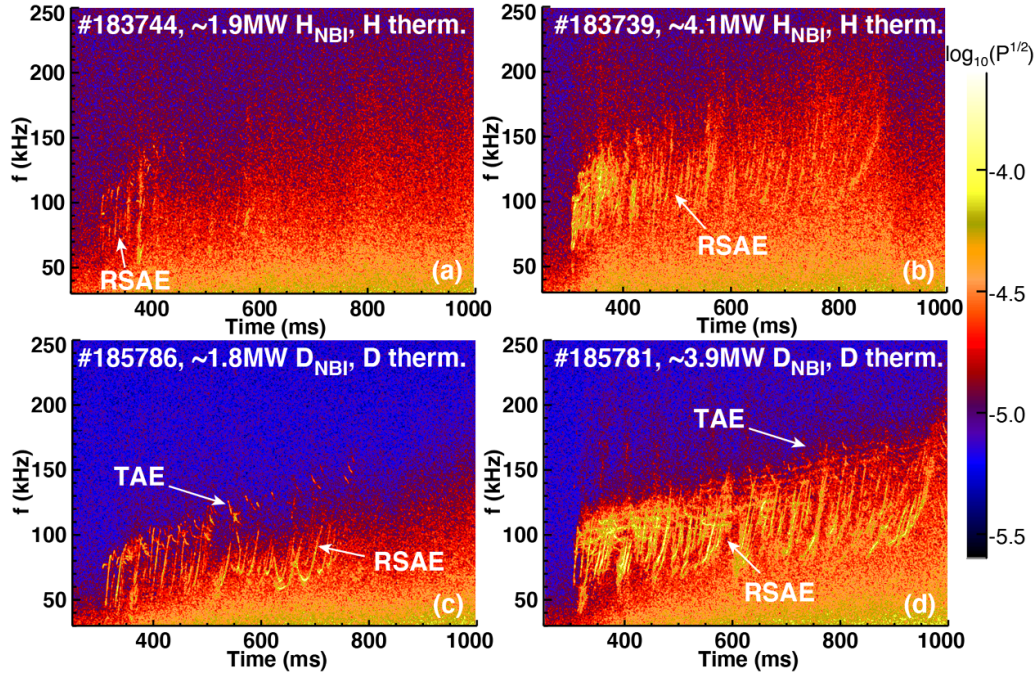


Figure 3. CO2 interferometer crosspower spectrograms for (a) and (b) $H_{\text{NBI}}, H_{\text{therm}}$ and (c), (d) $D_{\text{NBI}}, D_{\text{therm}}$ power scan respectively. Note discharges 183739 and 185781 are the discharges shown in figure 2.

Alfvén Eigenmodes (RSAEs) [24]. Crosspower spectrograms of CO₂ interferometer measured line-integrated density fluctuations [25] showing the variety of modes that are driven are presented in figure 3. In general, a spectrum of RSAEs and TAEs are driven unstable with D beam injection (figures 3(c) and (d)) while primarily only RSAEs are driven unstable for the H beam cases investigated (figures 3(a) and (b)). In these figures, TAEs are identified through their relatively slow frequency variation near the top of RSAE frequency sweeps, whereas RSAEs sweep up much faster in a pattern that depends sensitively on q_{min} [24]. Further, for a given beam power, the driven AE amplitudes are always reduced with H beams relative to D, an effect dominated by the faster slowing down of H and lower $\beta_{\text{fast-cl}}$ (see figure 9) and something reproduced by modeling (see section 4).

Similar results are obtained for D and H beam injection into mixed background species. Figure 4 shows data from a set of discharges in which the target plasma was roughly an equal mix of D and H with $n_D/n_e \approx 52\% - 58\%$ for the cases shown. The cited concentration values were measured using two approaches. The first utilizes periodic D beam blips to look at the 2.5 MeV beam plasma neutron emission relative to pure D cases; a reduction in D targets shows up as a reduction in peak neutron signal [26]. The second approach utilized the DIII-D main ion charge exchange system to look at the ratio of H to D brightness [27, 28]. In these discharges, the modes driven by H beams appear to be larger amplitude than those in pure H for a given power. D beams in contrast are similar or slightly weaker than pure D cases. In both cases, the types of modes identified are the same as the corresponding pure H or D cases.

Interestingly, the concentration values cited in figure 4 are further confirmed through the AEs themselves using so-called ‘AE spectroscopy’ [29]. In figure 5 the upper end of the RSAE frequency sweeps (approximately the TAE frequency) have been highlighted. Due to the mass dependence of the Alfvén speed, the ratio of TAE frequencies between the $n_D/n_e \approx 5\%$ and $n_D/n_e \approx 53\%$ should result in a ratio of TAE frequencies $\approx (1.53/1.05)^{1/2} = 1.21$ which is approximately what is observed. For ITER and future reactors, this mass dependence of the AE frequencies could potentially be used to identify the evolution of the D/T concentration in the core of *otherwise similar* plasmas in which AEs are unstable [30].

To quantify the change in mode amplitudes for the different isotope configurations, interferometer measurements of coherent mode amplitude are used. The DIII-D CO2 interferometer system consists of four chords [31], three vertical and one radial on the device midplane; the layout is shown in figure 6(a). In DIII-D EP experiments, typically crosspower spectra of the V2 and R0 chords are used to get a global overview of mode activity; these are the spectra shown in figures 3–5. TAEs like those identified in figures 3 and 4 are known to produce larger line-integrated density perturbations on vertically viewing interferometer chords than radial views with a similar tangency radius [25, 32], while their ballooning nature makes them appear more readily on the V2 and V3 chords. RSAEs, located at q_{min} , only appear on the innermost chords which traverse their location; as such, R0 is most effective for identifying RSAEs. Here, coherent modes are identified using a coherence analysis that finds frequencies and times at which the greater of the coherence between two sets of interferometer chords, the V2 and R0 chords and the V2 and V3 chords is

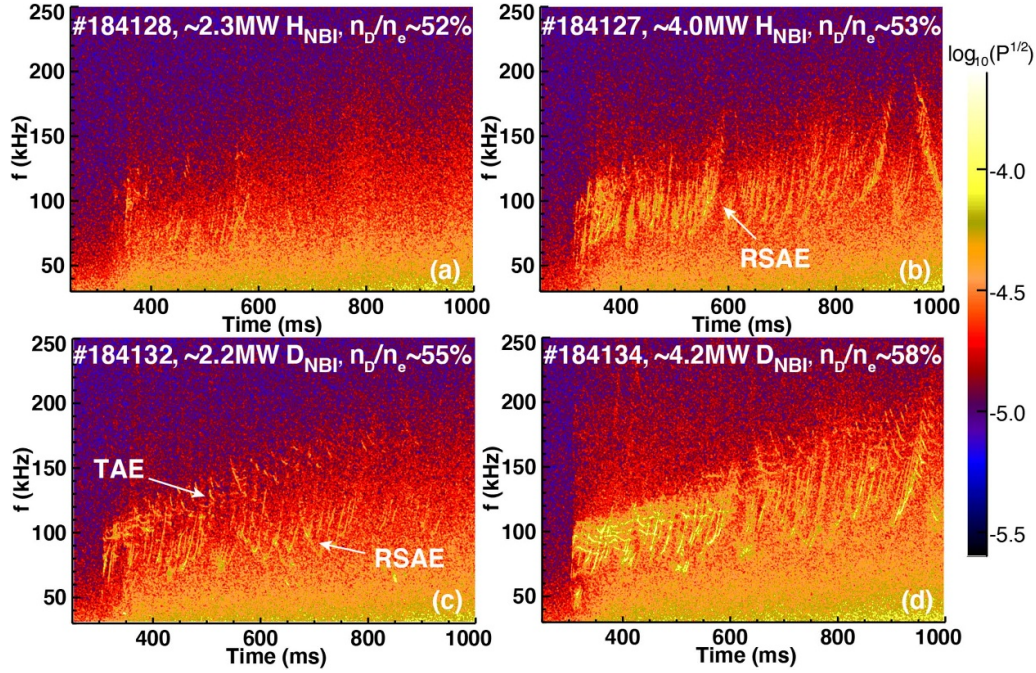


Figure 4. CO₂ interferometer crosspower spectrograms for (a) and (b) H_{NBI} , mixed H/D_{therm} and (c), (d) D_{NBI} , mixed H/D_{therm} power scan respectively.

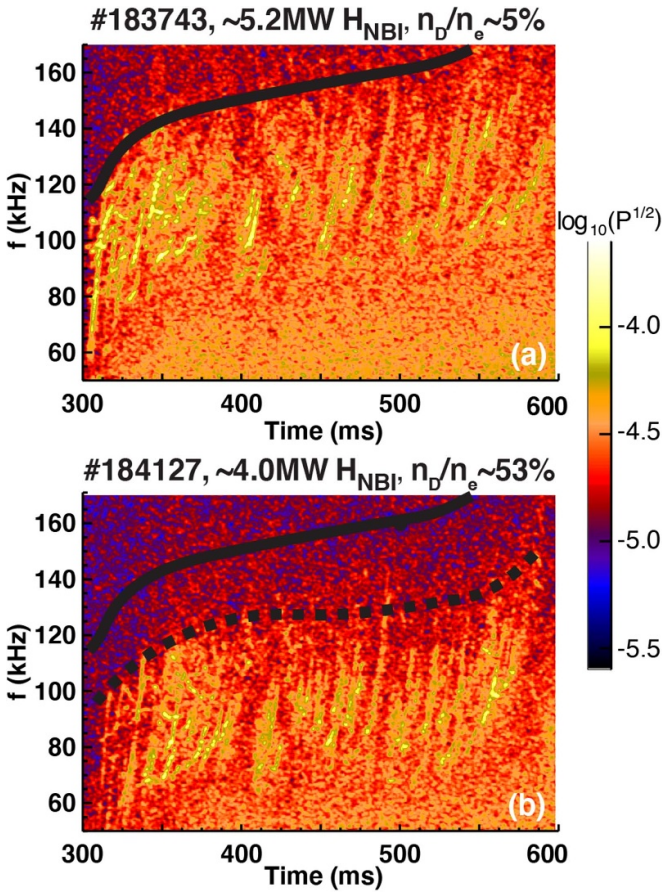


Figure 5. CO₂ interferometer crosspower spectrograms for (a) $H_{\text{NBI}}, H_{\text{therm}}$ and (b) H_{NBI} , mixed H/D_{therm} with approximate TAE frequencies overlaid (solid 183743 and dashed 184127)

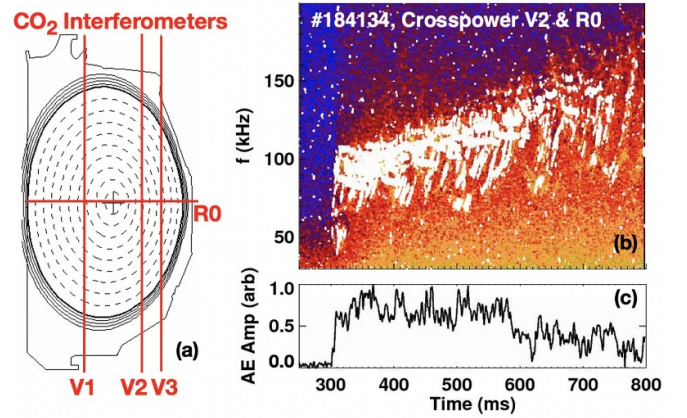


Figure 6. (a) DIII-D CO₂ interferometer layout. (b) spectrogram with coherent modes identified. (c) Inferred coherent AE amplitude.

above the 95% significance level [33]. An example of modes identified using this approach is given in figure 6(b). The AE amplitude discussed here is the integrated amplitude obtained from the crosspower of the V2 and R0 chords at times and frequencies identified using the coherence analysis, an example of which is given in figure 6(c). Due to the density evolution, for a comparison of amplitudes in the different conditions, amplitudes are scaled by line-averaged density at the relevant time to yield a quantity proportional to $\delta n_e/n_e$.

An important consideration in comparing the mode amplitudes and AE induced transport for the different discharges is the dependence of AE amplitude on safety factor (q) and the fact that q evolves differently in the different conditions,

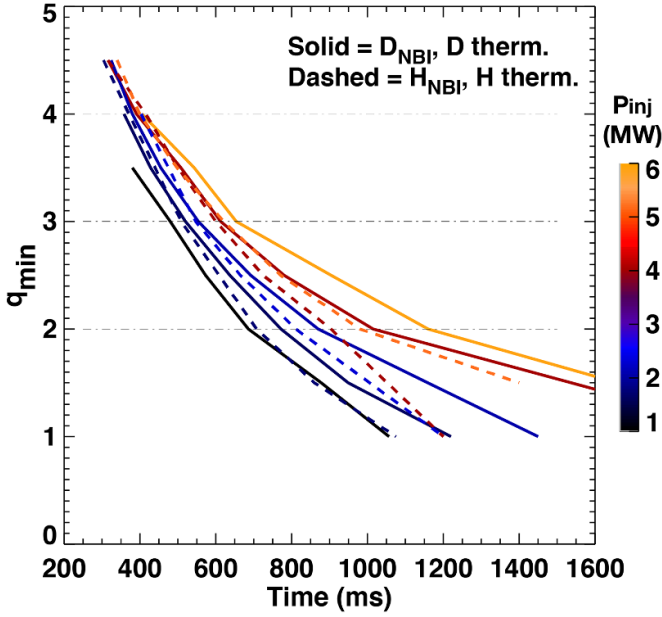


Figure 7. Temporal q_{\min} evolution for the different species and injected beam power cases used.

particularly when beam power is varied (a result of both different conductivity and current diffusion as well as neutral beam current drive variation). The temporal evolution for the different H_{NBI} into H_{thermal} and D_{NBI} into D_{thermal} cases is shown in figure 7, where q_{\min} values are obtained from RSAE spectroscopy as well as Internal Transport Barrier (ITB) timing [25, 34] and corroborated by Motional Stark Effect (MSE) [35] and magnetics-based equilibrium reconstructions. As can be seen from the spectrograms, the AE activity in each case evolves as the current penetrates which is ultimately due to a sensitivity to the minimum safety factor q_{\min} . To avoid conflating this dependence with that on species and drive power, the data presented in the comparisons that follow are collected around specific q_{\min} values rather than picking a specific time.

AE amplitudes for the different beam and thermal combinations are shown in figure 8(a) vs. injected power at $q_{\min} \approx 3$. AE amplitudes and beam power are averaged over 40 ms intervals and, in the case of H plasmas, more than a slowing down time away from any D beam diagnostic blips that occur. AE amplitude error bars represent the standard deviation of mode amplitudes over that interval. The trends visually apparent in the spectrograms are clarified in figure 8 and it is apparent that, for a given injected power and q_{\min} , H beams are significantly less efficient at driving AEs than D with a rough amplitude ordering of $H_{\text{NBI}} \rightarrow H < H_{\text{NBI}} \rightarrow H/D < D_{\text{NBI}} \rightarrow H/D < D_{\text{NBI}} \rightarrow D$. Interestingly, it is noted that over the range of conditions investigated, no transition in the nonlinear mode evolution was observed, i.e. from steady frequency modes to chirping, as in [14]. Here chirping does not refer to equilibrium induced frequency sweeping exhibited by RSAEs. This difference may be a result of the sub-Alfvénic beams used in DIII-D as compared to the super-Alfvénic beams described in [14].

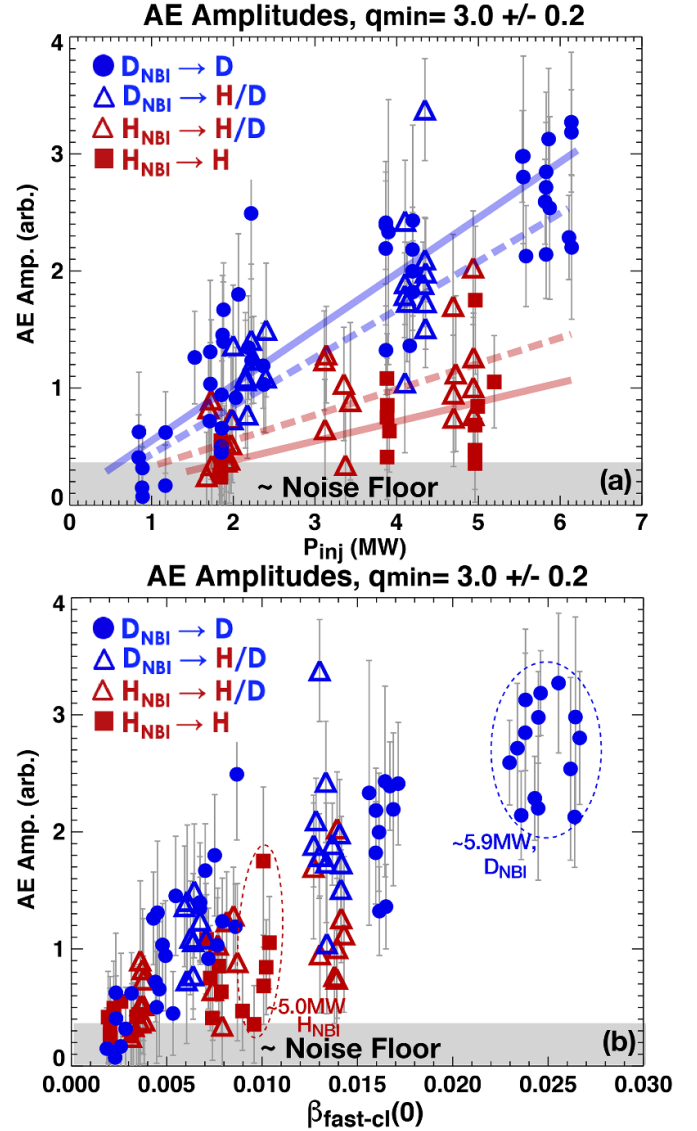


Figure 8. (a) AE amplitude vs. P_{inj} near $q_{\min} = 3$. (b) AE amplitude vs. $\beta_{\text{fast-cl}}(0)$ near $q_{\min} = 3$.

TRANSP calculations indicate that the dominant mechanism contributing to the difference between H and D beam driven AE activity is the faster classical slowing down of H beam ions relative to D due to the lighter H mass ($\tau_{\text{slow}} \approx M_{\text{fast}}$) and the resultant lower beam ion pressure. This can be seen in figure 8(b), where the AE density fluctuation amplitude calculated from CO2 interferometer chords is plotted for the various experimental beam and thermal species combinations vs. on-axis classical fast ion beta ($\beta_{\text{fast-cl}}(0)$), i.e. that expected in the absence of MHD. For a given classical beam ion pressure (rather than injected beam power), the AE amplitudes are comparable for H and D beam injection. This is in contrast to comparisons for similar injected power where a large variation exists for H_{NBI} and D_{NBI} mode amplitude, highlighted by comparing the circled data points for ≈ 5.0 MW H_{NBI} and ≈ 5.9 MW D_{NBI} . For these two cases, the $\beta_{\text{fast-cl}}$ varies by a factor of 2.5, similar to that of the average mode amplitude. Physically, for a given plasma shape, $\beta_{\text{fast-cl}}$ can

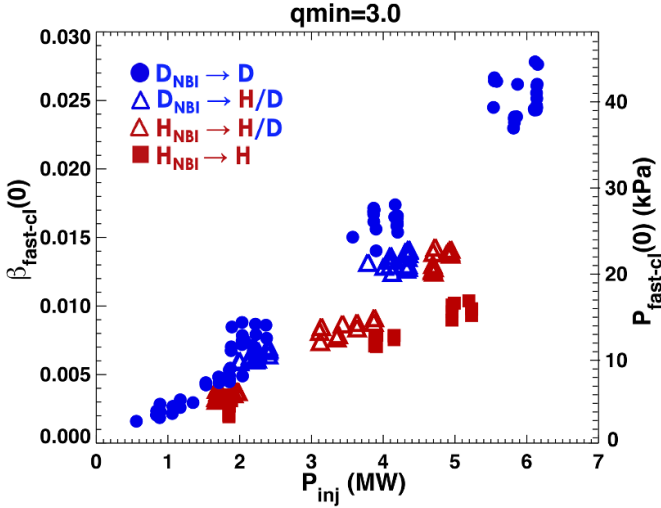


Figure 9. $\beta_{\text{fast-cl}}$ vs. P_{inj} for the different species and injected beam power cases used.

be thought of as representing the approximate average classical beam ion pressure gradient—the AE ‘standard drive’ mechanism [6].

The actual variation of $\beta_{\text{fast-cl}}$ with injected beam power for the various isotope combinations shown in figure 8 is given in figure 9. Note, the $\beta_{\text{fast-cl}}$ values given in figure 9 capture the amplitude trends across all species including mixed background plasmas. For example, comparison of the ≈ 3 – 5 MW cases shows an ordering of $\beta_{\text{fast-cl}}$ analogous to that observed for mode amplitudes at a given injected power, $H_{\text{NBI}} \rightarrow H < H_{\text{NBI}} \rightarrow H/D < D_{\text{NBI}} \rightarrow H/D < D_{\text{NBI}} \rightarrow D$. While other factors could also be at play, such as the fact that $H_{\text{NBI}} \rightarrow H/D$ has a higher Alfvénic Mach number than all other combinations and $D_{\text{NBI}} \rightarrow H/D$ has lower Alfvénic Mach number than $D_{\text{NBI}} \rightarrow D$, the data are consistent with a large role of $\beta_{\text{fast-cl}}$.

Figure 10 further illustrates this effect through a comparison of two repeat discharges with different electron densities varying by a factor of $2 \times$ during the current ramp. For the higher density, no AEs are unstable. In terms of beam ion slowing down physics, this doubling of density is roughly equivalent to halving the injected power or $\beta_{\text{fast-cl}}$. This is similar to taking the 4 MW $H_{\text{NBI}} \rightarrow H/D$ (Red open triangles) in figure 8(a) and moving them to the 2 MW points, which are in the noise. Alternatively, one would expect doubling the electron density in discharge 184127 would result in spectra similar to figure 4(a), except slightly lower mode amplitudes—which indeed is observed (figure 10(b)).

The relative dependence of AE amplitudes and stability on both q_{min} and $\beta_{\text{fast-cl}}$ is shown in figure 11, where the relative size of the markers is indicative of mode amplitude. The size of the black markers is indicative of the noise floor. As can be clearly seen, mode amplitudes increase as both q_{min} and beam ion pressure increases with very low amplitude or stable operating space below a line connection approximately

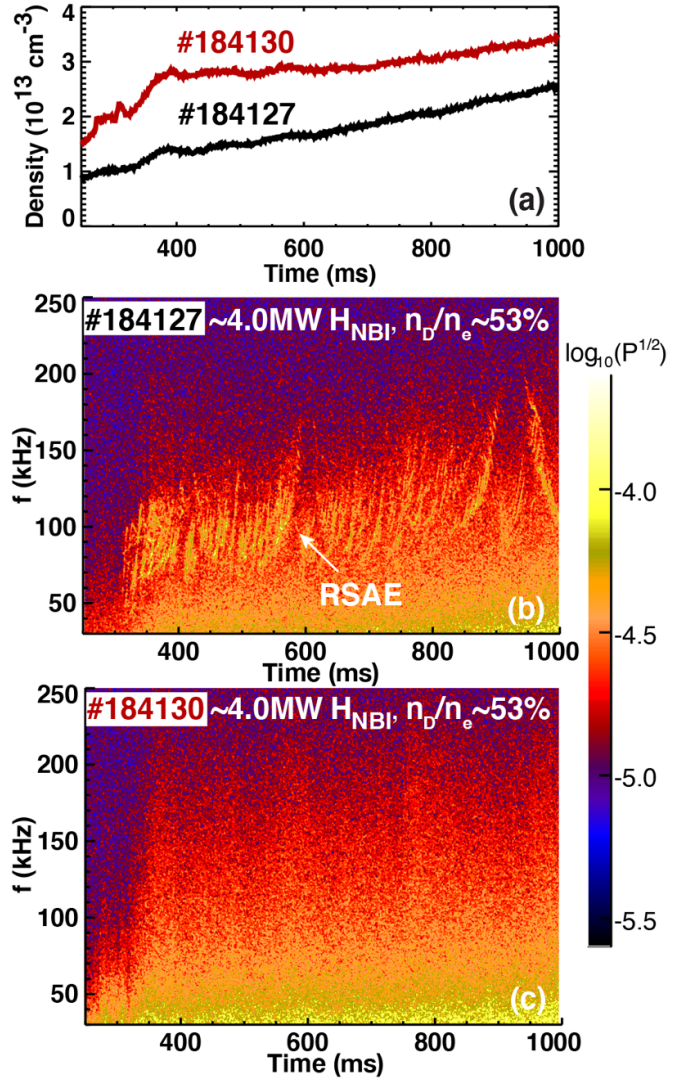


Figure 10. (a) Line-averaged density in DIII-D discharges 184127 and 184130. (b) and (c) CO₂ interferometer crosspower spectrograms for H_{NBI} , mixed H/D thermal at nominal and high density respectively.

$\beta_{\text{fast-cl}} = 0.002, q_{\text{min}} = 3$ and $\beta_{\text{fast-cl}} = 0.011, q_{\text{min}} = 1$. These data are consistent with a similar plot obtained using a larger database of 38 DIII-D D discharges focused on the impact of electron cyclotron heating on AE activity [36]. In general, RSAE activity typically dominates the unstable spectra near the stable/unstable boundary and TAEs are observed further into the unstable region. For experimental planning, data such as that presented in figure 11 can be used to guide DIII-D AE control experiments and scenario projections targeting AE stable operating points.

Theoretically, the most unstable toroidal mode number depends on fast ion Larmor radius and banana width [9, 11], and should scale with beam ion mass roughly as $n_{\text{max}} \approx 1/M_{\text{fast}}^{1/2}$ [9]. Cursory analysis (not shown) using the RSAE frequency model described in [36] to identify toroidal mode numbers, in for example the spectra of figure 4, appears to yield very similar range of unstable mode numbers for both H and D

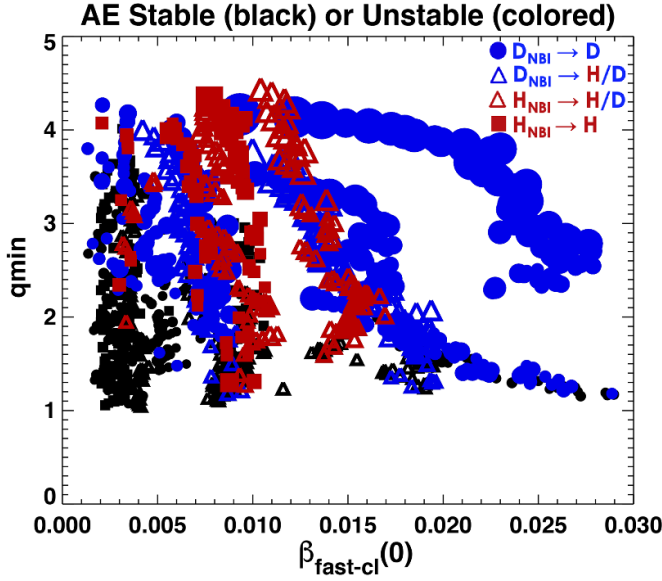


Figure 11. AE amplitude data plotted vs. q_{\min} and $\beta_{\text{fast-cl}}$. Marker size is linearly scaled according to mode amplitude from noise to max amplitude. Black indicates inferred amplitudes below noise floor.

beam injection. Roughly $n = 2 - 6 +$ (the exact range depends on beam power and q_{\min}) are routinely observed for each with $n = 2 - 4$ being the strongest. Attempts to extract any systematic differences between the two beam ion species for similar $\beta_{\text{fast-cl}}$ and q_{\min} were inconclusive, potentially due to the relatively low toroidal mode numbers observed to be most unstable.

4. MEGA modeling of AE activity

Computational modeling of the AE instability isotope dependencies is carried out using delta-F calculations with the hybrid MHD code MEGA [23]; and many of the important trends are reproduced. MEGA is a hybrid kinetic-MHD code, that includes energetic particles, which has successfully modeled AE stability and transport in DIII-D scenarios like those presented here [37–40]. For this application, fast ions are included using a delta-F particle-in-Cell approach for the gyrokinetic markers with an anisotropic slowing down form for the distribution function prescribed with similar numerical parameters to that described in [24]. The isotope experiments described here are simulated using experimental equilibria and kinetic profiles from the H beam injection into H thermal case 183739 (See figure 3(b) with a time chosen near $q_{\min} = 3$).

To simulate the power dependence, the on-axis fast ion pressure is scanned and the unstable spectrum observed. To simulate the isotope dependence, both the beam and thermal species are then switched to D and a second scan carried out. For this scan, $n = 3$ is chosen since that corresponds to a toroidal mode number frequently observed in these

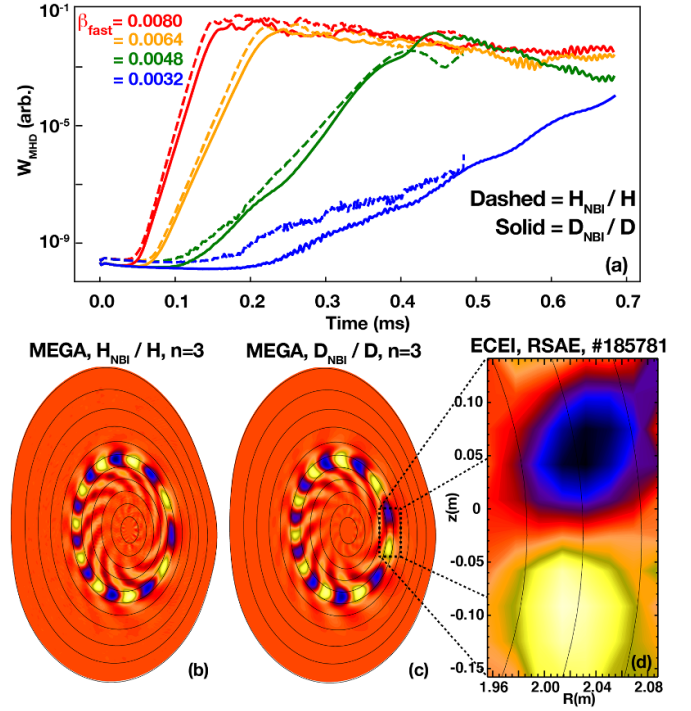


Figure 12. MEGA $n = 3$ results. (a) MHD energy vs. species and fast ion beta. (b) and (c) radial velocity (proportional to displacement and δT_e) at $t = 0.3$ ms for H_{NBI}/H and D_{NBI}/D . (d) ECEI for D_{NBI}/D case.

discharges [24]. MEGA calculations given in figure 12 show comparable growth rates (inferred from the slope of the temporal amplitude evolution) for H_{NBI} and D_{NBI} for the same on-axis β_{fast} , similar to the mode amplitude dependence on $\beta_{\text{fast-cl}}$ (NOT injected power) as shown in figure 8(b). An example comparison of the predicted RSAE eigenmode structure and that observed by 2D electron cyclotron imaging (ECEI) is given in figures 12(c) and (d), where good agreement is found including localization, extent and poloidal mode number.

The dependence on q_{\min} is investigated in a series of multi- n simulations in which the input q -profile and q_{\min} is scanned from $q_{\min} = 3.4 - 2.4$ by adjusting total current at fixed β_{fast} . Multi- n runs, as opposed to a single n , are used to reduce sensitivity to changes in mode type or existence for a specific n value that could cause abrupt changes in growth rate and a failure to see the overall trend toward reduced growth rate as q_{\min} decreases. The results of this numerical experiment are given in figure 13, where figures 13(a)–(f) shows the mode growth for $n = 1 - 6$ respectively and figure 13(g) shows the corresponding q -profiles used. Clearly, mode growth rates (a proxy for mode amplitudes) are extremely sensitive to q_{\min} with the relatively small change in q_{\min} ($q_{\min} = 3.4 - 2.4$) causing up to a factor of five reduction in growth rates for some cases. This modeling reinforces the approach to compare mode amplitudes and stability for a given q_{\min} as done in figure 8.

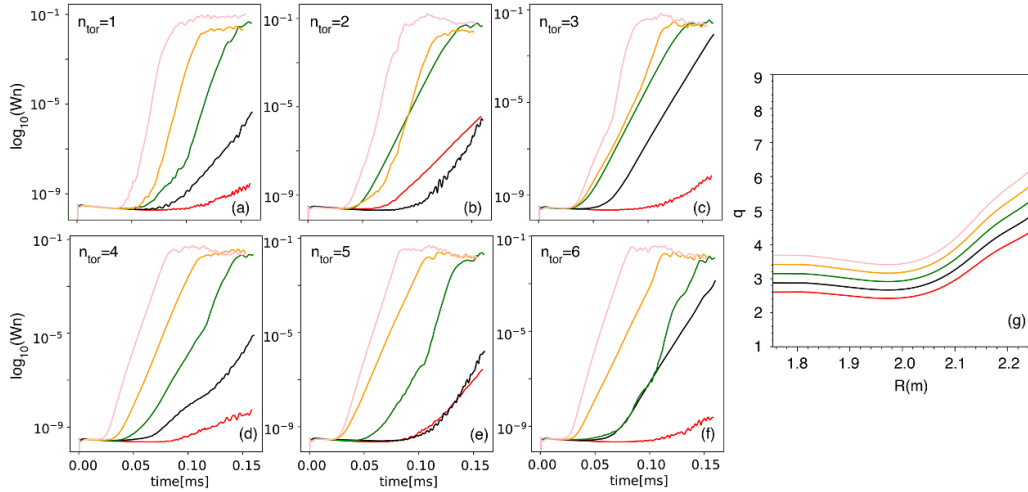


Figure 13. MEGA multi- n calculations showing mode growth dependence on q_{min} at $\beta_{\text{fast}} = 0.8\%$. (a)–(f) $n = 1 - 6$, (g) q -profiles. The different colors correspond to different q_{min} values.

5. Impact of isotope on AE induced EP transport and comparison with TGLFEP+TRANSP modeling

In this section, the effect of unstable AEs on the fast ion content is investigated. Figure 14 shows the experimentally measured stored energy obtained from EFIT [41] equilibrium reconstructions vs. $\beta_{\text{fast-cl}}$ for the different isotope combinations collected at $q_{\text{min}} = 4$ and $q_{\text{min}} = 3$ (figures 14(a) and (b) respectively). Overlaid on each plot are the classical predictions for total stored energy from TRANSP (W_{cl}). As input, TRANSP takes the measured thermal kinetic profiles ($n_e, T_e, T_i, n_{\text{imp}}, \text{rotation}$) along with beam heating waveforms; the thermal ion density is obtained from charge balance taking into account the measured electron and impurity densities as well as the calculated fast ion profile. Thus, any measured deficit in stored energy from ‘classical’ is primarily a deficit in fast ion stored energy. A deficit in measured fast ion stored energy from classical expectations can arise due to additional transport that leads to either complete loss of fast ions from the plasma or simply movement to regions of lower T_e (or higher n_e although densities are either centrally peaked or flat in these cases). The data in figure 14 show a significant departure from classical predictions as $\beta_{\text{fast-cl}}$ is increased. As with the mode amplitudes, the departure from classical at a given $\beta_{\text{fast-cl}}$ is similar for the different isotope combinations although the highest $\beta_{\text{fast-cl}}$ values are limited to D beam injection due to power limitations with H beams. As q_{min} is decreased, the fractional deficit is also decreased, again as expected from the measured decrease in mode amplitudes with q_{min} .

The measured stored energy for each case can be directly compared to both pre (see figure 1) and post experiment TGLFEP+Alpha calculations as shown in figure 15. In this figure, panels 1(a) and (b) show the measured total stored energy scaled to classical vs. $\beta_{\text{fast-cl}}$ at $q_{\text{min}} = 4$ and $q_{\text{min}} = 3$ respectively. By scaling to the classical expectation and plotting vs. $\beta_{\text{fast-cl}}$, issues associated with deviations of the actual kinetic profiles obtained in the experiment relative to those

used for the pre-experiment calculations are minimized. For example, the actual electron densities in the experiment were somewhat lower than that used for the pre-experiment calculations ($\approx 15\% - 25\%$) so, as elucidated in figure 10, comparison at a given power would be misleading because a higher $\beta_{\text{fast-cl}}$ (mode drive) was realized for a given injected power in the actual experiment. Post experiment TGLFEP+Alpha calculations use the measured kinetic profiles and equilibrium for the ≈ 4 MW cases in each isotope at $q_{\text{min}} = 3$ and scale the classical source rate as well as current to assess the impact at varying $\beta_{\text{fast-cl}}$ as well as q_{min} . Pre experiment calculations were carried out over a fixed injected power range, which is apparent in the reduced $\beta_{\text{fast-cl}}$ range for the H relative to D cases.

The calculations are found to capture the major trends well. In both cases, the D and H results lie very close to one another for a given $\beta_{\text{fast-cl}}$ – a confirmation of the fact that the dominant difference between these different isotope cases, in the parameter range investigated, is the classical slowing down. Essentially rescaled versions of these plots are shown in figures 15(c) and (d), where the measured total stored energy minus the classical thermal energy ($W - W_{\text{therm-cl}}$) scaled to the classical fast ion stored energy ($W_{\text{fast-cl}}$) over the same $\beta_{\text{fast-cl}}$ and q_{min} values are shown. The rationale for plotting the data in this manner is that since $W_{\text{therm-cl}}$ is essentially the measured thermal energy and W is the total stored energy, the difference is the measured fast ion stored energy; scaling to classical directly shows the deficit in fast ion stored energy. While the error bars are large, particularly at low $\beta_{\text{fast-cl}}$, where the total fast ion energy is only a very small fraction of the total stored energy, the calculations reproduce the measured transport with up to 60% deficits observed in the highest power D cases shown. The data are too noisy to tell whether the small predicted differences between H and D at a given $\beta_{\text{fast-cl}}$ are observed. The difference between isotopes for a given injected power, however, is contained in the $\beta_{\text{fast-cl}}$ scaling, indicating that this dependence is reproduced (this will be shown more

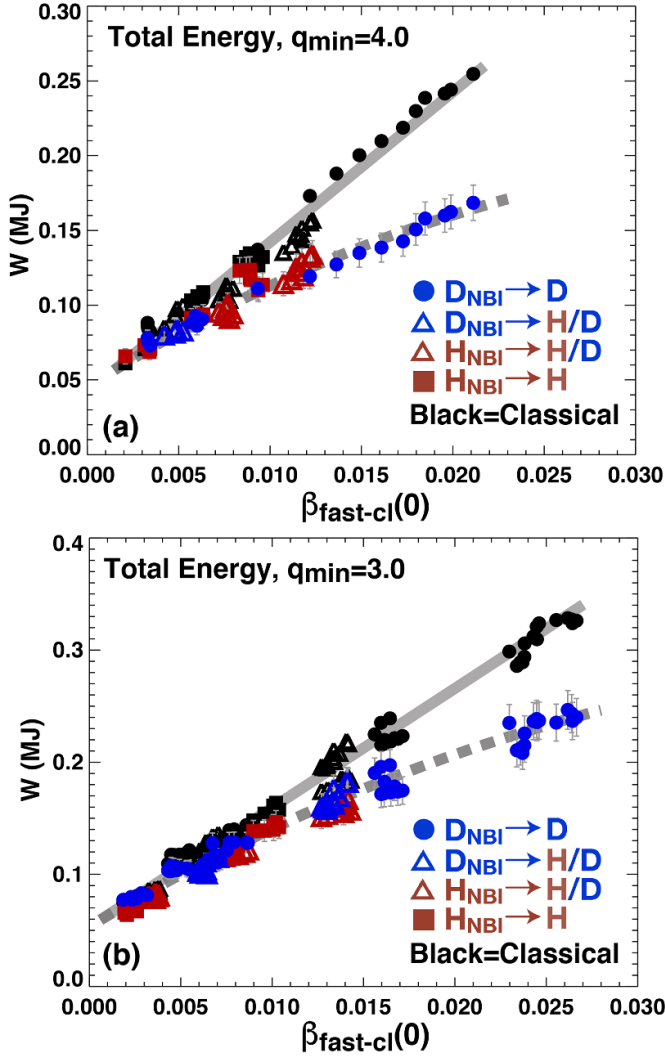


Figure 14. Total stored energy classical and measured vs. $\beta_{\text{fast-cl}}$ for (a) $q_{\min} \approx 4$ and (b) $q_{\min} \approx 3$. Overlaid solid/dashed gray lines are included to guide the eye for classical and measured values respectively.

clearly in discussion of figure 16). The fact that pre experiment calculations show significant transport even at $\beta_{\text{fast-cl}}$ values as low as 0.002 (and H powers as low as $P_{\text{inj}} \approx 1$ MW in figure 1) indicate they are likely too pessimistic and underestimate the threshold at which deleterious AE activity sets in. As can be seen in figure 3(a), even H beam cases with 2 MW of injection show little to no AE activity and, as shown in figure 8, amplitudes at these power and $\beta_{\text{fast-cl}}$ values are close to the noise floor. The difference between pre and post experiment calculations, and the higher predicted $\beta_{\text{fast-cl}}$ for effects to become noticeable in the post experiment case, is a result of modifications to the TGLFEP model itself including increased instability discrimination. Only modes driving energy flux primarily in the fast-ion channel (at least 10 times greater than in the thermal-ion channel) were considered. Additionally, the threshold growth rate was set to $\gamma_{\text{thresh}} = 0.15\gamma_E/|\hat{s}|$, where γ_E is the (generally small in this case) local $E \times B$ shearing rate

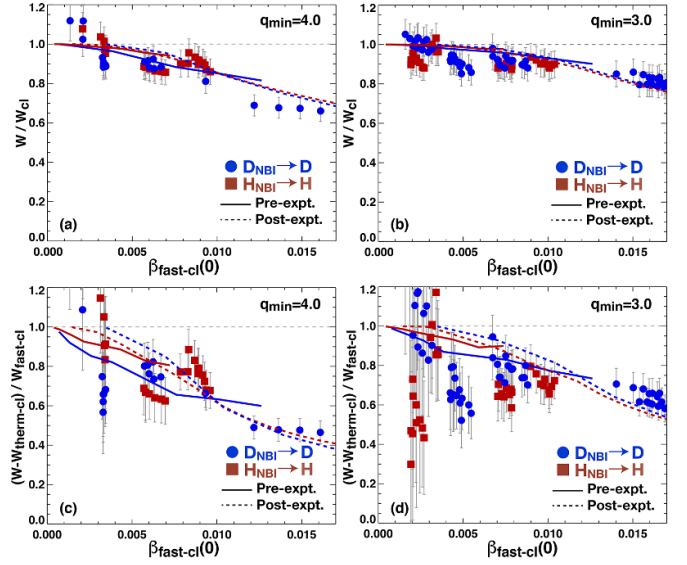


Figure 15. Total measured stored energy scaled to classical at (a) $q_{\min} \approx 4$ and (b) $q_{\min} \approx 3$, and comparison to pre-experiment and post-experiment calculations (solid and dashed respectively). Difference of total measured stored energy and thermal classical scaled to classical fast ion stored energy at (c) $q_{\min} \approx 4$ and (d) $q_{\min} \approx 3$.

and \hat{s} is the magnetic shear, as described in [42]. A nominally small cap is placed on γ_{thresh} near the q_{\min} surface where it would otherwise diverge. These updates to the TGLFEP selection algorithm were quantitatively significant, but do not change the qualitative picture and will be discussed in more detail in future publications.

Post experiment TGLFEP+Alpha calculations that used the actual measured experimental profiles can be compared directly to the unscaled stored energy deficits. These comparisons are shown in figure 16 for $q_{\min} = 4, 3$ and 2, where excellent quantitative agreement of both the power dependence and isotope dependence are found. While results with mixed D/H thermal plasma are shown, no TGLFEP calculations were carried out for those cases; they are provided for reference.

An additional point of comparison to TGLFEP modeling for D cases is possible, i.e. the DD 2.5 MeV neutron rates. A difference in DD neutron emission relative to classical TRANSP indicates larger than expected fast ion transport of the highest energy particles near the central high T_e region of the plasma, this is in contrast to the fast ion stored energy which has a much broader weight function [43]. Figure 17 shows the measured neutron emission and stored energy scaled to classical TRANSP predictions in black for the ≈ 4 MW $D_{\text{NBI}} \rightarrow D$ discharge 185781. As can be seen, the neutron deficit reaches 45% while the stored energy deficit is less ($\approx 27\%$); both decrease in time as q_{\min} evolves and the AE activity dissipates. Overlaid in red are the results of TRANSP runs that incorporate a time and radially dependent diffusivity derived from TGLFEP calculations. The TGLFEP+TRANSP calculations are much closer to unity, particularly for the stored

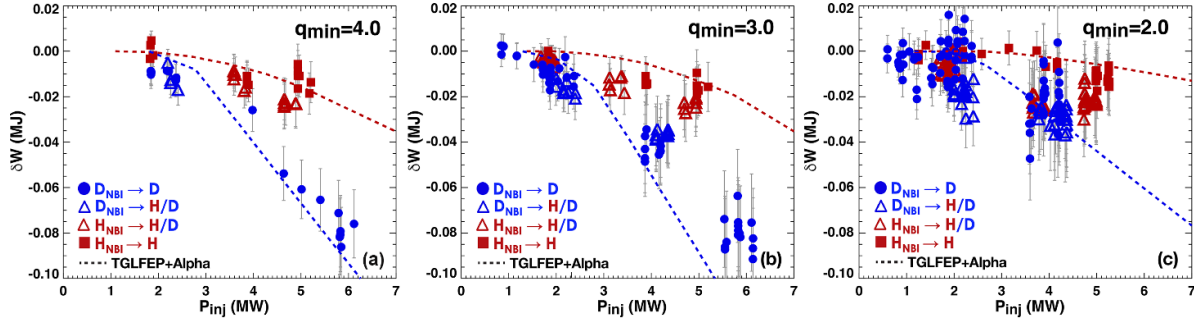


Figure 16. Measured deficit in stored energy vs. P_{inj} compared to TGLFEP+Alpha calculations at (a) $q_{min} \approx 4$, (b) $q_{min} \approx 3$ and (c) $q_{min} \approx 2$.

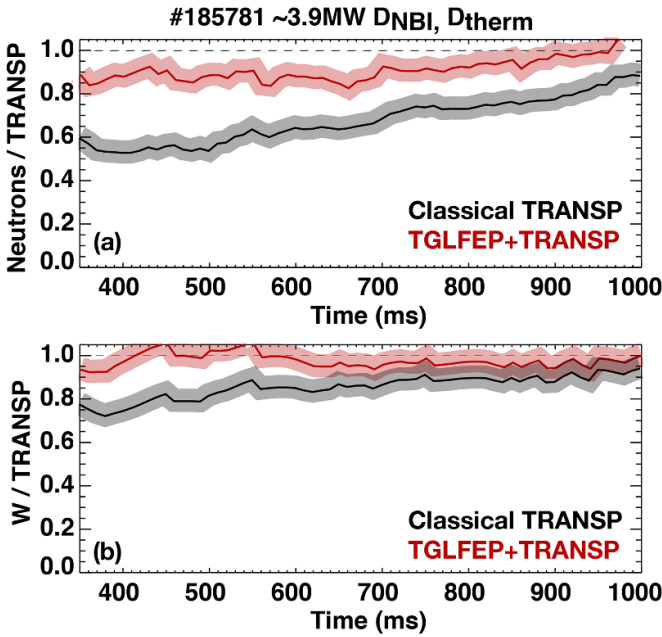


Figure 17. Measured (a) DD neutron emission and (b) stored energy scaled to TRANSP calculations without (black) and with (red) time-dependent diffusivity calculated by TGLFEP for D/D case 185781.

energy, indicating the relaxed fast ion profiles are closer to those obtained experimentally. The difference from unity in the neutron emission for the TGLFEP+TRANSP run indicates the transport of highest energy central fast ions causing the bulk of the DD neutron emission is somewhat underpredicted. This discrepancy is reasonable and likely due to limitations of the model, which assumes an energy independent diffusivity profile.

6. Summary and conclusions

Measurements of beam driven AE activity in matched D and H DIII-D plasmas as well as mixed background ($\approx 50/50$ D/H) plasmas with reversed magnetic shear which show a large difference in the driven mode amplitudes and spectra for a given injected beam power have been presented. In all cases with H beam injection, no TAEs and overall lower AE amplitudes

were observed, while cases with D beam injection can exhibit a mix of RSAEs and TAEs (an effect likely resulting from the lower maximum drive that could be tested with H). A comparison of mode amplitudes at a given q_{min} and classical on-axis fast ion pressure or $\beta_{fast-cl}$, indicate similar amplitudes are driven for all isotope combinations. This similar dependence on $\beta_{fast-cl}$ was also found in MEGA simulations through comparison of AE growth rates in H and D beam heated plasmas. These results indicate the dominant mechanism contributing to the observed difference between H and D beam drive is the faster classical slowing down of H beam ions relative to D and the resultant lower beam ion pressure—a result consistent with previous experiments in monotonic shear plasmas showing weaker or no AE activity with H beam injection [8, 13]. Similar results are found for deficits in stored energy due to the AEs, i.e. comparable transport is found for the different isotope combinations for a given $\beta_{fast-cl}$.

This experiment was also a ‘predict-first’ experiment in that TGLFEP+TRANSP was used to make estimates of the expected fast ion transport for the different isotope combinations. In general the major trends discussed above were predicted and the impact of AEs on stored energy relative to classical predictions was found to be in agreement with experiment, although pre experiment calculations indicated significant transport should set in at lower power values than observed experimentally. Post experiment calculations of the AE induced stored energy deficits using the reduced critical gradient model TGLFEP are in excellent quantitative agreement with the dependence on injected power, isotope and q_{min} —showing promise for rapid predictions of fast ion transport in future fusion devices.

Acknowledgments

This material is based upon work supported in part by the U.S. Department of Energy, Office of Science, Office of Fusion Energy Sciences, using the DIII-D National Fusion Facility, a DOE Office of Science user facility, under Awards DE-FC02-04ER54698, DE-AC02-09CH11466, DE-FG02-99ER54531, DE-SC0023500, DE-SC0018108 and DE-SC0020337. This report was prepared as an account of work sponsored by an agency of the United States Government. Neither the United States Government nor any agency thereof, nor any

of their employees, makes any warranty, express or implied, or assumes any legal liability or responsibility for the accuracy, completeness, or usefulness of any information, apparatus, product, or process disclosed, or represents that its use would not infringe privately owned rights. Reference herein to any specific commercial product, process, or service by trade name, trademark, manufacturer, or otherwise, does not necessarily constitute or imply its endorsement, recommendation, or favoring by the United States Government or any agency thereof. The views and opinions of authors expressed herein do not necessarily state or reflect those of the United States Government or any agency thereof.

ORCID iDs

M.A. Van Zeeland  <https://orcid.org/0000-0002-7911-2739>
 X.D. Du  <https://orcid.org/0000-0001-6127-2825>
 W.W. Heidbrink  <https://orcid.org/0000-0002-6942-8043>
 C. Chrystal  <https://orcid.org/0000-0003-3049-8658>
 C. Crocker  <https://orcid.org/0000-0003-2379-5814>
 G. DeGrandchamp  <https://orcid.org/0000-0002-1363-9570>
 S. Haskey  <https://orcid.org/0000-0002-9978-6597>
 J. Gonzalez-Martin  <https://orcid.org/0000-0002-3237-5195>
 K.E. Thome  <https://orcid.org/0000-0002-4801-3922>
 G. Yu  <https://orcid.org/0000-0002-0002-5342>

References

- [1] Heidbrink W.W. et al 2014 *Plasma Phys. Control. Fusion* **56** 095030
- [2] Holcomb C.T. et al 2015 *Phys. Plasmas* **22** 055904
- [3] Bass E.M. and Waltz R.E. 2020 *Nucl. Fusion* **60** 016032
- [4] Spong D.A., Bass E.M., Deng W., Heidbrink W.W., Lin Z., Tobias B., Van Zeeland M.A., Austin M.E., Domier C.W. and Luhmann N.C. 2012 *Phys. Plasmas* **19** 082511
- [5] Taimourzadeh S. et al 2019 *Nucl. Fusion* **59** 066006
- [6] Rosenbluth M.N. and Rutherford P.H. 1975 *Phys. Rev. Lett.* **34** 1428
- [7] Heidbrink W.W. and Sadler G.J. 1994 *Nucl. Fusion* **34** 535–615
- [8] Strait E.J., Heidbrink W.W., Turnbull A.D., Chu M.S. and Duong H.H. 1993 *Nucl. Fusion* **33** 1849–70
- [9] Heidbrink W.W. 2002 *Phys. Plasmas* **9** 2113
- [10] Nazikian R. et al 1997 *Phys. Rev. Lett.* **78** 2976
- [11] Seo J. et al (JET contributors) 2020 *Nucl. Fusion* **60** 066008
- [12] Fasoli A., Jaun A. and Testa D. 2000 *Phys. Lett. A* **4** 288
- [13] Borba D., Alper B., Budny R.V., Fasoli A., Heeter R.F., Kerner W., Sharapov S.E. and Smeulders P. 2000 *Nucl. Fusion* **40** 775
- [14] Gusev V.K. et al 2015 *Nucl. Fusion* **55** 104016
- [15] Heidbrink W.W. et al 2021 *Nucl. Fusion* **61** 106021
- [16] Tinguely R.A. et al 2023 *IAEA FEC EA-CN-316 EX-W/1996*
- [17] Sheng H., Waltz R.E. and Staebler G.M. 2017 *Phys. Plasmas* **24** 072305
- [18] Poli F., Sachdev J., Breslau J., Gorelenkova M. and Yuan X. 2018 TRANSP (v18.2.) *Computer software* (<https://doi.org/10.11578/dc.20180627.4>)
- [19] Pankin A., McCune D., Andre R., Bateman G. and Kritiz A. 2004 *Comput. Phys. Commun.* **159** 157
- [20] Staebler M., Kinsey J.E. and Waltz R.E. 2005 *Phys. Plasmas* **12** 102508
- [21] Staebler G.M., Kinsey J.E. and Waltz R.E. 2007 *Phys. Plasmas* **14** 55909
- [22] Collins C.S., Heidbrink W.W., Austin M.E., Kramer G.J., Pace D.C., Petty C.C., Stagner L., Van Zeeland M.A., White R.B. and Zhu Y.B. 2016 *Phys. Rev. Lett.* **116** 95001
- [23] Todo Y. and Sato T. 1998 *Phys. Plasmas* **5** 1321
- [24] Van Zeeland M.A., Kramer G.J., Austin M.E., Boivin R.L., Heidbrink W.W., Makowski M.A., McKee G.R., Nazikian R., Solomon W.M. and Wang G. 2006 *Phys. Rev. Lett.* **97** 135001
- [25] Van Zeeland M.A. et al 2006 *Nucl. Fusion* **46** S880–7
- [26] Heidbrink W.W., Miah M., Darrow D., LeBlanc B., Medley S.S., Roquemore A.L. and Cecil F.E. 2003 *Nucl. Fusion* **43** 883
- [27] Haskey S.R., Stagner L., Grierson B.A., Chrystal C., DeGrandchamp G.H., Heidbrink W.W., Van Zeeland M.A. and Vincena S. 2021 *Rev. Sci. Instrum.* **92** 043535
- [28] Grierson B.A., Burrell K. H., Chrystal C., Groebner R.J., Kaplan D.H., Heidbrink W.W., Muñoz Burgos J.M., Pablant N.A., Solomon W.M. and Van Zeeland M.A. 2012 *Rev. Sci. Instrum.* **83** 10D529
- [29] Holties H.A., Fasoli A., Goedbloed J.P., Huysmans G.T.A. and Kerner W. 1997 *Phys. Plasmas* **4** 709
- [30] Fasoli A., Testa D., Sharapov S., Berk H.L., Breizman B., Gondhalekar A., Heeter R.F. and Mantsinen M. (contributors to the EFDA-JET Workprogramme) 2002 *Plasma Phys. Control. Fusion* **44** B159
- [31] Carlstrom T.N., Ahlgren D.R. and Crosbie J. 1988 *Rev. Sci. Instrum.* **7** 1063
- [32] Van Zeeland M.A., Kramer G.J., Nazikian R., Berk H.L., Carlstrom T.N. and Solomon W.M. 2005 *Plasma Phys. Control. Fusion* **47** L31
- [33] Ferron J.R. and Strait E.J. 1992 *Rev. Sci. Instrum.* **63** 4799
- [34] Austin M.E. et al 2006 *Phys. Plasmas* **13** 082502
- [35] Rice B.W., Nilson D.G., Burrell K.H. and Lao L.L. 1999 *Rev. Sci. Instrum.* **70** 815
- [36] Van Zeeland M.A. et al 2016 *Nucl. Fusion* **56** 112007
- [37] Todo Y., Van Zeeland M.A., Bierwage A. and Heidbrink W.W. 2014 *Nucl. Fusion* **54** 104012
- [38] Todo Y., Van Zeeland M.A., Bierwage A., Heidbrink W.W. and Austin M.E. 2015 *Nucl. Fusion* **55** 073020
- [39] Todo Y., Van Zeeland M.A. and Heidbrink W.W. 2016 *Nucl. Fusion* **56** 112008
- [40] Van Zeeland M.A. et al 2021 *Nucl. Fusion* **61** 066028
- [41] Lao L.L., St John H., Stambaugh R.D., Kellman A.G. and Pfeiffer W. 1985 *Nucl. Fusion* **25** 1611
- [42] Bass E.M. and Waltz R.E. 2017 *Phys. Plasmas* **24** 122302
- [43] Heidbrink W.W., Luo Y., Burrell K.H., Harvey R.W., Pinsker R.I. and Ruskov E. 2007 *Plasma Phys. Control. Fusion* **49** 1457–75